RESEARCH ARTICLE

Editor's Choice

ADVANCED
MATERIALS
TECHNOLOGIES

www.advmattechnol.de

Deep-Learning-Assisted Triboelectric Whisker Sensor Array for Real-Time Motion Sensing of Unmanned Underwater Vehicle

Bo Liu, Bowen Dong, Hao Jin, Peng Zhu, Zhaoyang Mu, Yuanzheng Li, Jianhua Liu, Zhaochen Meng, Xinyue Zhou, Peng Xu,* and Minyi Xu*

Aquatic animals can perceive their surrounding flow fields through highly evolved sensory systems. For instance, a seal whisker array understands the hydrodynamic field that allows seals to forage and navigate in dark environments. In this work, a deep learning-assisted underwater triboelectric whisker sensor array (TWSA) is designed for the 3D motion estimation and near-field perception of unmanned underwater vehicles. Each sensor comprises a high aspect ratio elliptical whisker shaft, four sensing units at the root of the elliptical whisker shaft, and a flexible corrugated joint simulating the skin on the cheek surface of aquatic animals. The TWSA effectively identifies flow velocity and direction in the 3D underwater environments and exhibits a rapid response time of 19 ms, a high sensitivity of $0.2 V/ms^{-1}$, and a signal-to-noise ratio of 58 dB. The device also locks onto the frequency of the upstream wake vortex, achieving a minimal detection accuracy of 81.2%. Moreover, when integrated with an unmanned underwater vehicle, the TWSA can estimate 3D trajectories assisted by a trained deep learning model, with a root mean square error of ≈ 0.02. Thus, the TWSA-based assisted perception holds immense potential for enhancing unmanned underwater vehicle near-field perception and navigation capabilities across a wide range of applications.

1. Introduction

Maneuverable unmanned underwater vehicles play a crucial role in various underwater operations, including oceanographic research, maritime search and rescue, environmental monitoring, etc.[1–4] Robust capabilities of the flow field perception are necessary for these vehicles to perform effectively.[5,6] While optical and acoustic sensors can offer flow field perception, their performance is constrained within the intricate underwater operation environment.[7–9] For instance, the detection signal of optical sensors is disrupted by significant scattering noise caused by the intense scattering properties of seawater, which can compromise both the accuracy and range of perception.[10,11] Acoustic sensors are affected by multipath effects, self-noise, and ambient ocean noise, resulting in a low signal-to-noise ratio and a high loss of sensing signals.[12,13] Moreover, both underwater optical and acoustic sensors exhibit limited perception proficiency in the near field of unmanned underwater vehicles. Perception information includes the speed of the unmanned underwater vehicle, water flow, nearby obstacles, and wakes.[14] Thus, developing novel flow field perception technology is necessary to enhance the near-field perception capabilities of underwater vehicles.

Aquatic animals have developed sophisticated sensory capabilities to enhance their perception of surrounding flow fields.[15] For example, the lateral line system in fish senses velocity and pressure fluctuations in the surrounding flow field to avoid obstacles,[16,17] while electric fish detect weak electric field changes in the flow fields to locate prey.[18] Particularly, seal whiskers have been the focus of recent studies due to their exceptional ability to sense surrounding flow fields, enabling seals to forage and navigate in dark environments.[19–21] The design of bionic whisker devices for sensing flow fields around underwater vehicles utilizes various sensing modalities, including piezoresistive, triboelectric, microelectromechanical,[22–25] capacitive, and magnetostrictive technologies. These sensors are installed on underwater vehicles to detect flow velocity, identify and track wakes, and avoid obstacles. However, applying a single whisker-inspired sensor does not fully replicate the function of real seal whiskers. This necessitates an ultra-sensitive whisker array to enhance the perception dimensions for underwater vehicles.

B. Liu, B. Dong, H. Jin, P. Zhu, Z. Mu, Y. Li, J. Liu, Z. Meng, X. Zhou, M. Xu
Dalian Key Lab of Marine Micro/Nano Energy and Self-powered Systems
Marine Engineering College
Dalian Maritime University
Dalian 116026, China
E-mail: xuminyi@dlmu.edu.cn
P. Xu
Intelligent Biomimetic Design Lab
College of Engineering
Peking University
Beijing 100871, China
E-mail: pengxu@pku.edu.cn

**ADVANCED
SCIENCE NEWS**

www.advancedsciencenews.com

**ADVANCED
MATERIALS
TECHNOLOGIES**

www.advmattechnol.de

Triboelectric nanogenerators (TENGs) utilize the combination of triboelectric electrification and electrostatic induction effects to convert mechanical energy into electrical energy.[26–29] Their primary advantage lies in their ability to transform weak disturbances into high-amplitude electrical signals.[30–33] Leveraging the benefits of TENG, a range of TENG sensors has been developeds.[34,35] For example, the artificial tactile sensing system developed by integrating TENG with tactile perception provides a new dimension of sensing for intelligent devices.[36,37] These systems introduce new perceptual dimensions to smart devices and amalgamate various sensory modalities, including vision, thereby improving the recognition accuracy of these devices.[38] Besides, TENG is also applied in various underwater scenarios, including constructing underwater observation networks, monitoring fish behavior, identifying the shapes of underwater targets, and aiding underwater vehicle navigation.[39–41] Additionally, whisker-inspired TENG sensors have been widely developed to track wakes, detect flow velocity, and assist in obstacle avoidance for underwater vehicles.[42,43] In reality, a seal whisker array can accurately acquire 3D flow field information, enabling the tracking of prey movement paths and the sensing of flow field environments for navigation.[44–46] However, challenges remain in using whisker-inspired TENG sensors for flow field perception in underwater vehicles. Developing a bionic TENG-based whisker array for passive detection 3D hydrodynamic fields is significant for decreasing the perception gap between artificial whiskers and real seal whiskers.

In this study, a bionic underwater triboelectric whisker sensor array (TWSA) was designed for passive near-field flow perception, further endowing unmanned underwater vehicles to estimate motion path and obstacle information with the aid of a deep learning (DL) model. The TWSA comprises an array of four sensors arranged as shown in Figure S1 (Supporting Information). Each sensor includes a high aspect ratio (0.403) elliptical whisker shaft, four sensing units at the root of the elliptical whisker shaft, and a flexible corrugated joint that simulates the skin on the cheek surface of aquatic animals. In the steady flows experiment, the vibration frequency and amplitude of the whisker shaft were demonstrated to be determined by the flow velocity and the angle between the long axis of the elliptical whisker shaft and the direction of the flow field. In particular, the elliptical whisker shaft effectively suppresses flow-induced vibrations when the angle is 0. Utilizing this characteristic, the eddy current characteristics of the wake of the upstream spoiler are detected using a fast Fourier transform (FFT), achieving a detection accuracy greater than 80%. In addition, the device was installed on unmanned underwater vehicles, and the signal from the TWSA was mapped to the speed, angle, and obstacle estimation of the unmanned underwater vehicles through the DL model. The root mean square error (RMSE) was found to be 0.02, indicating that TWSA effectively perceives the near flow field of underwater vehicles and assists in 3D path and obstacle estimation.

2. Results and Discussion

2.1. Basic Structure and Working Mechanism of TWSA

Harbor seals possess ≈88 whiskers arranged in a complex array about the surface on both sides of their cheeks. Each whisker con-

tains a high-aspect-ratio elliptical whisker shaft and a richly innervated follicle as shown in Figure S2 (Supporting Information). Specifically, the transmission mode of neurons is illustrated in **Figure 1a**. As seals swim, the displacement generated by the elliptical whisker shaft is relayed by receptive cells located in the follicles at the whisker's base. This displacement is ultimately processed as fluid information in the seal's brain. Inspired by this mechanism, an artificial whisker array was developed and mounted on the head of underwater vehicles to assist in obtaining near-field information, as shown in Figure 1b. The specific structures and composition of the four sensors contained in the TWSA are illustrated in Figure 1c and Figure S3 (Supporting Information). Each sensor is composed of a high-aspect-ratio elliptical shaft and a sensing module at its base, measuring 40 mm in height and 20 mm in diameter. The elliptical whisker shaft has a long axis measuring 12.4 mm and a short axis measuring 5 mm featuring a carbon fiber rod. Additionally, the sensing module primarily consists of a watertight base crafted from epoxy resin adhesive, a gas chamber comprising a silicone shell and polylactic acid (PLA) holder, four triboelectric sensing units (20 mm × 10 mm), and a central PLA ball with a metal memory spring. Specifically, primary components for sealing TWSA include a watertight base crafted from epoxy and a flexible corrugated joint shell made from silicone rubber (Ecoflex 30). Notably, the flexible corrugated joint shell ensures water-tightness and supports the internal air chamber of TWSA, providing ample airtight space for the sensing units. The outermost layer of four triboelectric sensing units was wrapped with a silicone shell connected to a back plate of a base, providing support and fixation. In addition, a metal memory spring was positioned at the center of the base, with a PLA ball featuring a blind hole fixed atop it through a screwed hole. Specifically, the distance between the PLA ball and the sensing unit is 8 mm, as shown in Figure S4 (Supporting Information). Then the carbon fiber shaft of the whisker shaft was wedged into this blind hole. As depicted in Figure 1d, when subjected to external stimulation, the whisker shaft's carbon fiber rod drives the PLA ball to compress the silicone sleeve of the sensing unit. This compression evenly distributes force across the silicone rubber sleeve, causing deformation of the triboelectric sensing unit in the corresponding direction. Figure 1e depicts the configuration of the triboelectric sensing unit, which comprises Fluorinated Ethylene Propylene (FEP) films coated with conductive ink, a Chlorinated Polypropylene film to prevent electrostatic interference, and an outer flexible cover made from silicone rubber (Ecoflex 30). The conductive ink acts as both the electrode and the dielectric layer with positive electron affinity, whereas the FEP films serve as the dielectric layer with negative electron affinity. Importantly, the outermost layer of the sensor unit is sealed with Polytetrafluoroethylene (PTFE). PTFE's exceptional water resistance effectively insulates external water ions, preventing them from influencing charge transfer within the sensor unit.

As a result, the conductive ink comes into contact with the FEP film, leading to the overlapping of electron clouds between the two layers. Electrons migrate from the ink layer to the deeper potential well of the FEP film due to the higher electronegativity of FEP compared to ink, resulting in a voltage signal. When the external stimulation disappears from the whisker shaft, the elastic deformation of the silicone sleeve causes the FEP film to separate from the ink electrode. Due to the misalignment of
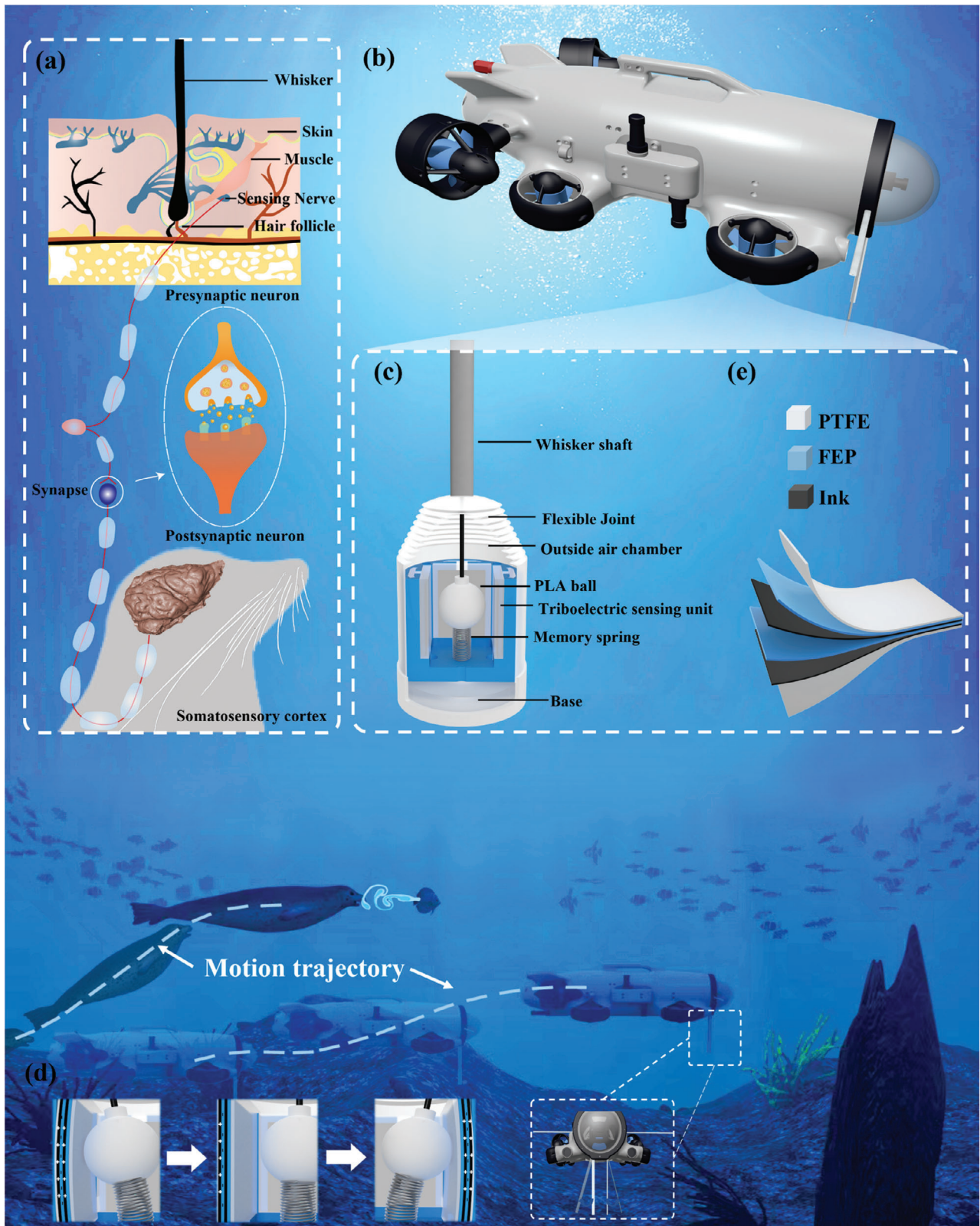
**ADVANCED
SCIENCE NEWS**

www.advancedsciencenews.com

**ADVANCED
MATERIALS
TECHNOLOGIES**

www.advmattechnol.de

Figure 1. Bionic principles, structure, and operating mechanisms of a bionic underwater triboelectric whisker sensor array (TWSA). a) Sensory principles of seal whiskers. b) Unmanned Underwater Vehicle(UUV) equipped with TWSA. c) Structural details of the TWSA. d) Working principle of the TWSA. e) Diagram of the sensing unit structure.

**ADVANCED
SCIENCE NEWS**

www.advancedsciencenews.com

**ADVANCED
MATERIALS
TECHNOLOGIES**

www.advmattechnol.de

positive and negative triboelectric charges on the same plane, this separation creates a dipole moment and potential difference between the two contact surfaces. Subsequently, free electrons flow through the external circuit to equilibrate the local electric field. This leads to a positive charge on the conductive ink electrode until the distance between the two contact surfaces is balanced. At this point, the contact films no longer generate triboelectrification or electrostatic induction. Eventually, the charge distribution reverts to its original state, thereby concluding the cycle. COMSOL Multiphysics is employed to validate the electrical potential distributions between the two triboelectric layers during operation, as illustrated in Figure S5 (Supporting Information). Particularly, the COMSOL simulation conditions were defined based on actual experimental data. The air boundary was established, the surface charge density was set to 10 μC m^{-2}, and a separation of 1 mm was maintained between the two films of the sensing unit.

2.2. Electrical Characterization of TWSA

Harbor seals can discern the velocity and direction of the flow field through their elliptical cross section whiskers in aquatic environments. This ability results from the dynamic properties of the whiskers, which are influenced by the flow velocity and the angle of attack between the whisker's major axis and the instantaneous direction of the flow. To investigate the specific performance of TWSA to perceive the velocity and direction of water flow within a stable flow field, it was mounted on the towing platform of the test water pool (6000 mm × 3000 mm × 1500 mm) as shown in **Figure 2a**. The motion of the towing platform along the X-axis and Y-axis is independently controlled by separate servo motors, with a speed range extending from 0 to 500mm s^{-1}. Figure S6 (Supporting Information) illustrates the experimental data acquisition system, which includes an amplifier, AD7606, and a minimal system board. The analog signal from the sensing unit, collected by the amplifier, is converted to a digital signal by the AD7606 and subsequently stored on the minimal system board.

The angle α varying from 0° to 90° between the major axis D of the elliptical whisker shaft and the flow field direction is defined as the attack angle, as depicted in Figure 2b. The eddy current characteristics of TWSA at different attack angles under a flow velocity of 300 mm s^{-1} were studied using ANSYS Fluent fluid-solid coupling simulation. As shown in Figure 2c, the simulation results indicate that no regular vortex street is formed behind the TWSA when $\alpha = 0°$ proving VIV is effectively suppressed. However, a regular vortex street gradually forms as the angle increases when the attack angle exceeds 30°, and the influence of vortex-induced vibrations (VIV) on the TWSA progressively increases. Additionally, the calculation domain and grid size are respectively shown in Figure 2d,e. Moreover, Figure 2f illustrates the variation in amplitude and frequency of TWSA's output signal with the attack angle at a flow velocity of 300 mm s^{-1}. Notably, the elliptical whisker shaft can effectively suppress VIV at attack angles ranging from 0° to 30° (small attack angles), resulting in low amplitude and frequency of the output signal. However, the elliptical whisker shaft exhibits significant amplitude vibrations as the attack angle increases and exceeds 30° (large attack angles)

consistent with the simulation results. Particularly, the amplitude increases rapidly with the attack angle, while the frequency grows slowly. When TWSA flows through a fluid with density (ρ) at velocity (v), the lift force (F_L) is modeled by the lift Equation (1).

$$F_L = \frac{1}{2} C_L \rho v^2 A_\alpha \tag{1}$$

$$A_\alpha = A \sin \alpha \tag{2}$$

$$A = D_X L \tag{3}$$

in which the lift coefficient (C) is determined by the shape and thickness of the whisker shaft. The projected area (A_α) of the whisker shaft in the direction of flow is determined by the height (L), width (D_X), and angle of attack (α) (from Equations 2 to 3).

Furthermore, Figure 2g,h presents the signal output from four sensing units and the dominant frequency signals derived through FFT analysis at a flow velocity of 300 mm s^{-1}. As steady flow circumvented the towed TWSA during transportation by the towing platform, asymmetrically arranged vortices periodically detached from both sides of the elliptical whisker shaft and moved in opposite directions. An asymmetrical vortex street generates a vortex-induced force on the elliptical whisker shaft, periodically causing the PLA ball to impact sensing units 1 and 3. Furthermore, sensing unit 4 is affected not only by the drag force FD from the towing platform but also by the movement of the PLA ball in the direction of sensing units 1 and 3. The drag force (F_D) was calculated with the following Equation (4):

$$F_D = \frac{1}{2} C_D \rho v^2 A_\alpha \tag{4}$$

where the lift coefficient (C_D) is determined by the shape and thickness of the whisker shaft. Although sensing unit 2 is not directly impacted by the PLA ball, vibrations from its movement periodically influence the signal in unit 2, resulting in the smallest amplitude among the units. The frequencies from 4 sensing units are approximately the same, primarily consisting of a fundamental frequency of 0.5 Hz due to flow resistance and a main frequency of 7.6 Hz from VIV. Moreover, the output voltage of sensing units 1 and 3 was identical, exhibiting a phase difference of 0.066 s. Furthermore, the outputs of sensing units 2 and 4 were lower than those of units 1 and 3, with unit 4 demonstrating a higher voltage magnitude than unit 2. Experimental and simulation results across various angles of attack reveal that TWSA can effectively suppress self-excited oscillations at a $\alpha = 0°$ angle of attack in a uniform flow field. Conversely, self-excited oscillations are not suppressed at $\alpha = 90°$. Consequently, subsequent research focuses exclusively on TWSA's capacity to sense the environmental flow field at $\alpha = 0°$, and analyzes the impact of TWSA''s motion on the output signal at $\alpha = 90°$.

ANSYS Fluent was used to explore the influence of velocity on TWSA's signal output at $\alpha = 90°$, as illustrated in Figure S7 (Supporting Information). Particularly, the ANSYS computational domain comprises 1.5 million mesh elements. The top, bottom, left, and right boundaries of the flow field are specified as symmetry planes, while the cylinder surface is defined as a no-slip wall. A velocity inlet condition is applied, with inlet velocities set at 100, 200, 300, 400, and 500 mm/s. The outlet is defined as a
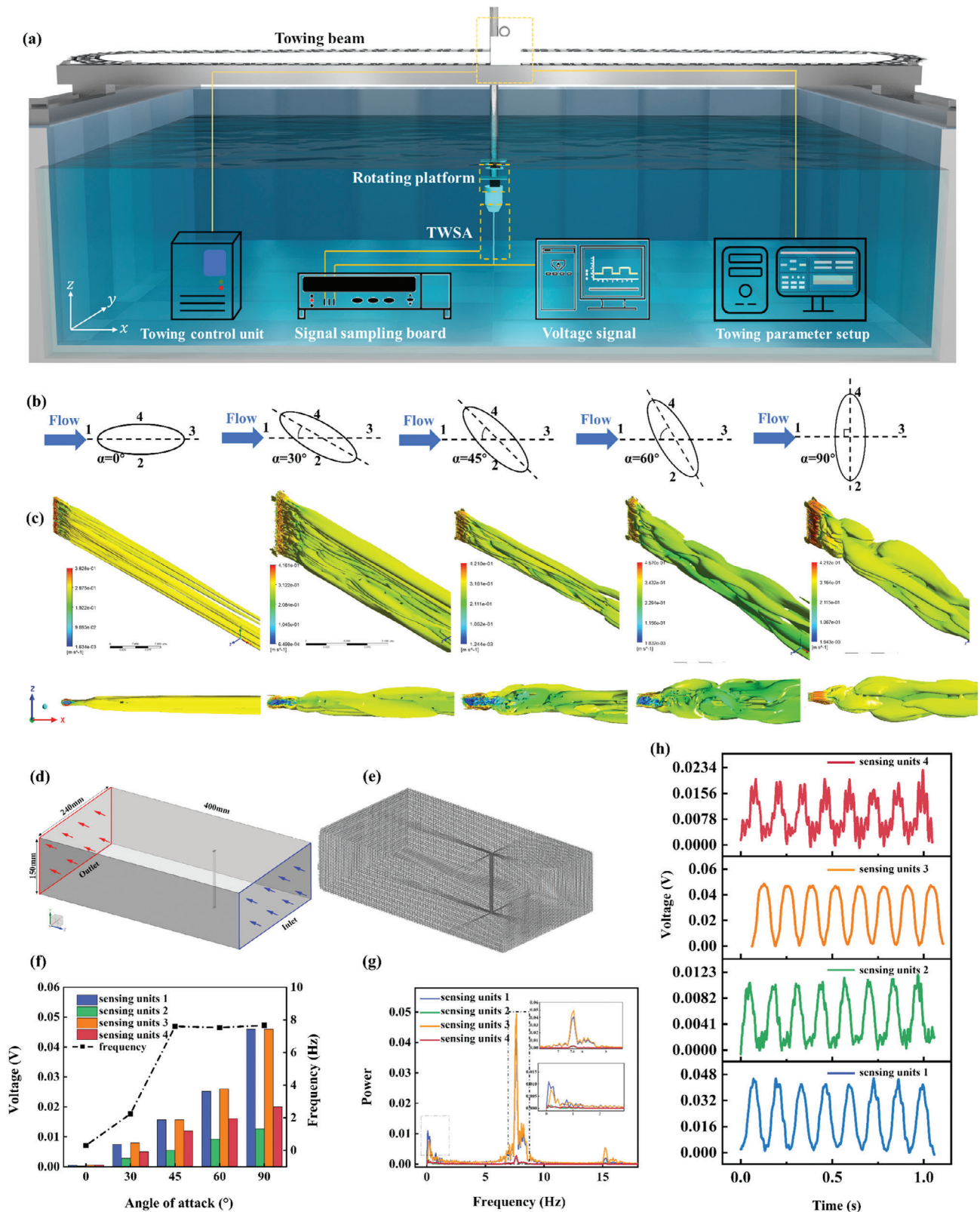
ADVANCED
SCIENCE NEWS

www.advancedsciencenews.com

ADVANCED
MATERIALS
TECHNOLOGIES

www.advmattechnol.de

Figure 2. Output characteristics of the TWSA under steady flow velocity. a) Experimental setup of the TWSA b) Schematic diagram of the whisker shaft at different angles of attack. c–e) Schematic diagram of ANSYS simulation. f) Fundamental frequency of the voltage signal from the TWSA in the case of attack angles ranging from 0° to 90°. g) Fundamental frequency of the voltage signals from the four sensing units. h) Voltage curve characteristics of four sensing units.
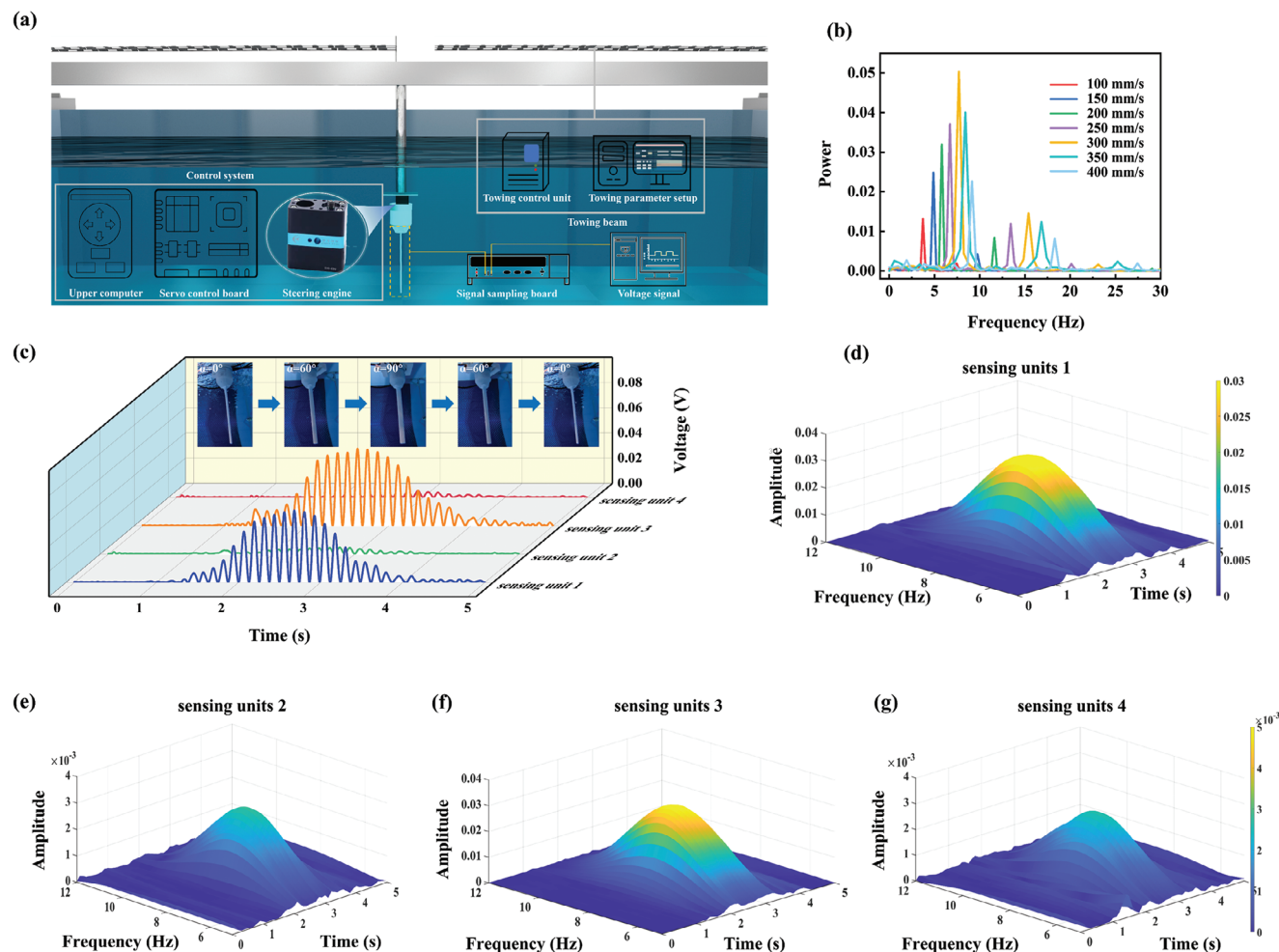
**ADVANCED
SCIENCE NEWS**

www.advancedsciencenews.com

**ADVANCED
MATERIALS
TECHNOLOGIES**

www.advmattechnol.de

Figure 3. TWSA measurement of continuously varying flow directions. a) Continuously varying flow directions experimental setup of the TWSA. b) Fundamental frequency of the voltage output from the TWSA at different flow velocities at $\alpha = 90°$. c) Voltage of TWSA during continuous changes of attack angle. d–g) Spectrogram of the four sensing units of the TWSA during continuous changes of attack angle.

pressure outlet with a gauge pressure of 0 Pa. The fluid is modeled as water, with a density of 998.2 kg m^{-3} and a dynamic viscosity of 0.001003 kg/(m s^{-1}). The SST turbulence model is employed for the simulation. The simulation of the flow field revealed that the frequency of the Karman vortex street behind TWSA significantly increases with increasing velocity. Additionally, TWSA was mounted on a rotating experimental platform with various motion speeds configured to simulate different water flow velocities, as shown in **Figure 3**a. Figure 3a,b shows the dominant frequency of TWSA's output signal as flow velocities increased, closely matching the simulation results. This evidence confirms that TWSA can effectively respond to variations in flow field velocities. A rotating test bench was utilized to simulate various flow directions to assess TWSA's ability to discern continuous motion direction. Figure 3c illustrates the signal output of the four sensing units as TWSA's attack angle continuously varies from 0° to 90°, then back to 0° at a flow velocity of 300 mm s^{-1}. During TWSA's motion, the amplitude of the signal output varies with the angle of attack. Specifically, as the attack angle shifts from 0° to 90°, the amplitude of the output signal progressively increases. However, the amplitude of the output signal progres-

sively decreases as the attack angle is reduced from 90° to 0°. Furthermore, the short-time Fourier transform (STFT) was applied to the output signal of four sensing units as depicted in Figure 3d–g. Notably, within the attack angle range from 0° to 30°, the dominant frequency of TWSA's signal increases with the increased attack angle. However, the dominant frequency change is minimal and stabilizes at ≈7.6 Hz between attack angles 30° and 90°. Additionally, the power spectral density of the output voltage varies in response to the different attack angles (see Video S1, Supporting Information). This experimental result demonstrates that changes in TWSA's motion velocity and direction can be discerned from its signal characteristics.

A Karman vortex street periodically forms behind a cylindrical when positioned in a uniform flow field. By analyzing the parameters of this vortex street, the characteristic properties of the cylindrical can be identified. Consequently, TWSA can measure the deflection of the whisker shaft caused by wake-induced vibrations (WIV) at $\alpha = 0°$. To investigate the relationship between the vibration response of TWSA and the shedding vortex characteristics, both TWSA and the cylinder were placed in a recirculating water flume equipped with Particle Image Velocimetry (PIV),
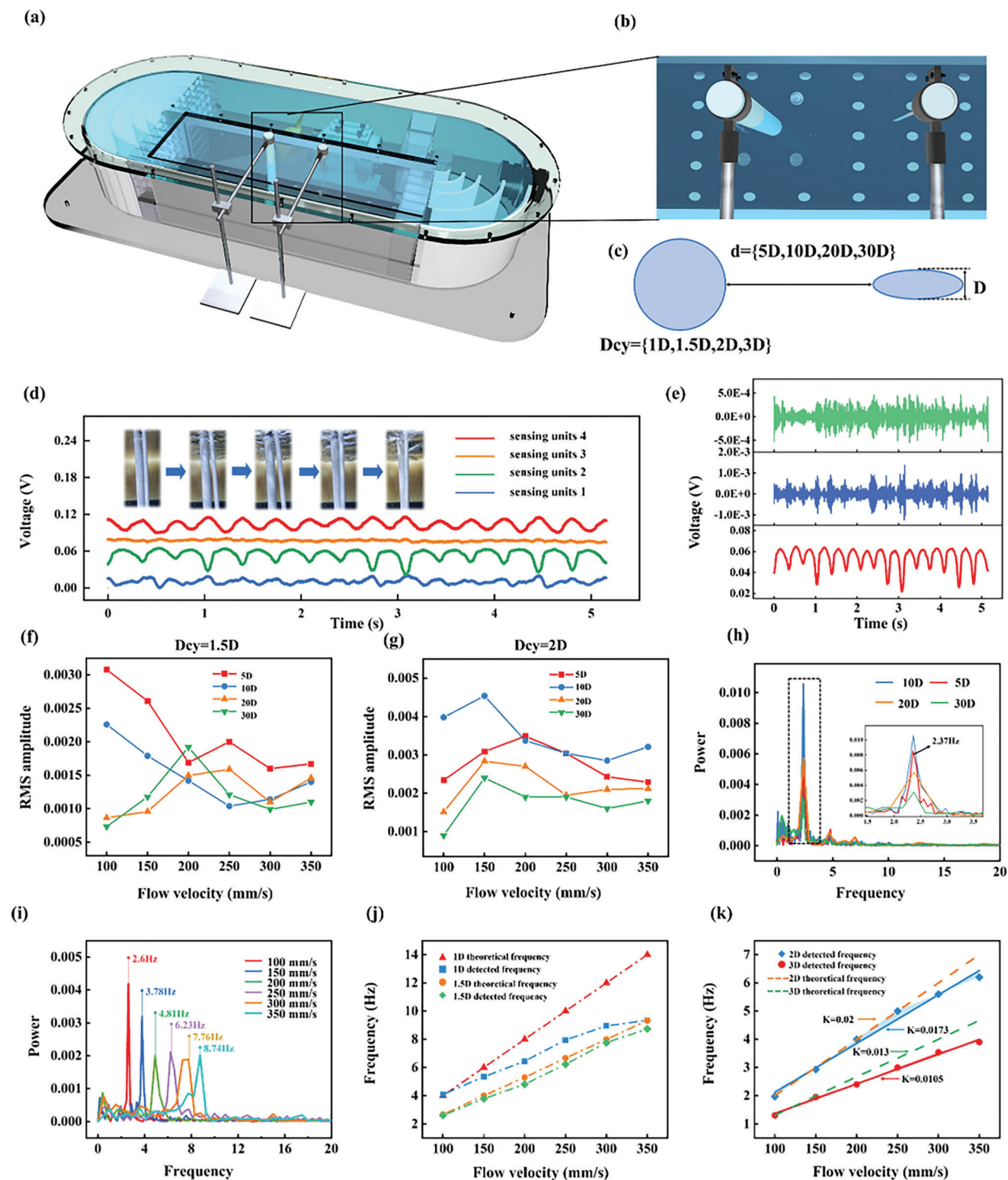
**ADVANCED
SCIENCE NEWS**

www.advancedsciencenews.com

**ADVANCED
MATERIALS
TECHNOLOGIES**

www.advmattechnol.de

Figure 4. Voltage output characteristics of the TWSA under wake-induced vibrations (WIV). a–c) Basic structures of experimental setup of the TWSA in WIV. d,e) Voltage output of four sensing units of TWSA. f,g) RMS amplitude of TWSA's output voltages for various flow velocities and distance(d). h) Fundamental frequency of the TWSA's voltage signal for different flow velocities. i) Frequency domain of the TWSA's voltage signal for different distance(d). j,k) Theoretical and detected dominant frequency of TWSA under various flow velocity.

**ADVANCED
SCIENCE NEWS**

www.advancedsciencenews.com

**ADVANCED
MATERIALS
TECHNOLOGIES**

www.advmattechnol.de

as illustrated in **Figure** 4a. Specifically, this recirculating water flume incorporates a motor, a guide plate, and a grid structure. The recirculating water flume dimensions are 900 mm × 400 mm × 250 mm. The motor speed is controlled by an AT2-0450X inverter, allowing flow rates to vary from 100 to 500 mm s^{-1}. The grid structure and guide plate ensure consistent flow field stability at the recirculating water flume's outlet. Additionally, PIV utilizes a SUMLINEG-8000 pulsed laser and an underwater camera operating at a sampling frame rate of 120 frames per second. The vortex structure behind the cylinder was captured using PIV to analyze the WIV of the cylinder at a flow velocity of 300 mm s^{-1}, as depicted in Figure S8 (Supporting Information). An increase in the size of the shedding vortex behind the cylinder was observed as the cylinder diameter increased, accompanied by a decrease in frequency. This phenomenon aligns with theoretical predictions of vortex-shedding frequency (Equation 5), where the Strouhal number (S_t) is defined as 0.2 for Reynolds numbers (Re) less than 3000.

$$f = S_t \frac{U}{D_{cy}} \tag{5}$$

For clarity, the minor axis diameter of the elliptical whisker shaft was designated as D (5 mm). Figure 4b,c shows the cylinder with diameters of Dcy = 1D, 1.5D, 2D, 3D (5, 7.5, 10, and 15 mm) is placed at d = 5D, 10D, 20D, 30D (25, 50, 100, and 150 mm) from the leading edge of TWSA respectively. Figure 4d presents the signal output of TWSA when the flow velocity is 300 mm s^{-1}, with the cylinder (Dcy = 2D) positioned at d = 10D. The elliptical whisker shaft is subjected to the combined effects of water flow resistance and WIV, which drive the PLA ball to impact the sensing units. Periodic oscillations induced by WIV predominantly influence sensing units 2 and 4, generating voltage signals with identical periods and amplitudes, but with phase differences of half a period between sensing units 2 and 4. Additionally, sensing units 1 and 3 are simultaneously influenced by water flow resistance and WIV, resulting in irregular output signals. This work is focused exclusively on the effect of WIV on the characteristics of signal output under varying values of d and Dcy. Therefore, subsequent analyses are primarily centered on the signal output amplitude and frequency from sensing units 2 and 4. Furthermore, the signal output from sensing unit 2 is decomposed using wavelet analysis, with decomposition results displayed in Figure 4e. The signal characteristics of sensing unit 2 components two components: a fundamental wave (red curves) with a frequency of 2.6 Hz from VIV, and high-frequency carrier waves (green curves and blue curves) from disturbances of the experience water pool. In addition, the output signal-to-noise ratio of ≈58 dB, and a response time of 19 ms (Figure S9, Supporting Information). This demonstrates that the TWSA possesses advantages such as a high signal-to-noise ratio and high sensitivity(0.2 V/ms^{-1}), effectively enabling the perception of cylindrical wake flows.

Figure 4f illustrates the variation in root mean square amplitude of TWSA at different d and flow velocities under conditions of a small-diameter fixed cylinder (D_{cy} = 1.5D). The excitation effects of upstream cylindrical vortices on TWSA gradually weaken as distance increases. Conversely, under conditions with a large-diameter fixed cylinder (D_{cy} = 2D, 3D), the root mean square am-

Table 1. Detection accuracy.

Flow Velocity [mm s^{-1}]	$D_{cy} = 1D$	$D_{cy} = 1.5D$	$D_{cy} = 2D$	$D_{cy} = 3D$
V = 100	84.6%	97.7%	98.5%	100%
V = 150	83.2%	94.5%	97.7%	97.5%
V = 200	82.3%	92.3%	100%	97.5%
V = 250	81.2%	94.4%	100%	89.9%
V = 300	–	97%	93.3%	87.5%
V = 350	–	94.2%	87.2%	84.7%

plitude of TWSA initially increases and then decreases with an increased distance d, as shown in Figure 4g and Figure S10a (Supporting Information). This occurs because TWSA resides in the recirculation zone of an upstream cylinder when the cylinder's diameter is large and the distance is short. The vibration of the TWSA is inhibited when TWSA and the upstream cylinder are in shear layer attachment mode. As the distance increases, excitation effects are enhanced by a shift to common vortex shedding mode. Further, excitation effects gradually diminish with further increased distance d. An increase in the diameter of an upstream cylinder leads to TWSA amplitude peaks occurring at higher flow rates when comparing changes across the sizes of three cylinders. For instance, the peak root mean square amplitude appears at a flow rate of 100 mm s^{-1} at D_{cy} = 1.5D, while the peak occurs at a flow rate of 150 mm s^{-1} and a cylinder diameter of 2D. Larger cylinder diameters result in larger trailing vortices and increased distance between adjacent vortices. Consequently, higher flow rates are required to achieve the vortex-shedding frequency necessary to match the natural frequency of TWSA. In summary, the vibratory response of TWSA exhibits a positive correlation with the size of the upstream cylinder and a generally negative correlation with the distance between the TWSA and the cylinder.

Additionally, Figure S10b (Supporting Information) and Figure 4h illustrate the dominant frequency characteristic of TWSA under varying values of Dcy and d. The dominant frequency of TWSA decreases from 5.1 to 2.35 Hz as Dcy decreases from 3D to 1D. However, varying d does not influence the dominant frequency of the TWSA signal output. Furthermore, Figure 4i displays FFT waveforms of TWSA signal output at different flow rates under experimental conditions of D_{cy} = 1.5D and d = 5D. The dominant frequency of TWSA increases from 2.6 to 8.74 Hz as the flow rate increases from 100 to 350 mm s^{-1}. Furthermore, Figure 4j and Figure S10c (Supporting Information) show the variation of the dominant frequency and theoretical frequency of the signal output of TWSA with the flow velocity under different D_{cy}. It demonstrated that TWSA can detect the vortex shedding frequency of the upstream cylinder under most flow velocity conditions, with the detected frequency closely matching the theoretical frequency as shown in Figure 4k and Figure S10d (Supporting Information). To quantitatively evaluate TWSA's perception ability of the wake, the theoretical frequency is defined as ft, and the measured frequency is defined as f_d. The correlation degree h between these two parameters is defined as the detection accuracy, as shown in **Table 1**. The overall detection accuracy (D_{ac})(Equation 6) of TWSA is higher than 81.2%. Besides, by comparing with conventional sensors, it can be seen

**ADVANCED
SCIENCE NEWS**

www.advancedsciencenews.com

**ADVANCED
MATERIALS
TECHNOLOGIES**

www.advmattechnol.de

Table 2. Comparisons on underwater whisker sensor for sensing flow field.

Reference	Sensing unit materials	Flow speed [ms^{-1}]	Wake flow	Attack angle
Our work	TENG	0–0.5	Yes	Yes
Liu et al.,	TENG	0–1	No	No
Stocking et al.,	Capacitance	0–1	No	Yes
Beem et al.,	Piezoresistor	0–0.6	Yes	No

from **Table 2** that TWSA has significant potential for application in flow field measurements.

$$D_{ac} = \left(1 - \frac{|f_d - f_t|}{f_t} \right) \times 100\% \qquad (6)$$

3. Demonstration

To further explore the perception capability of TWSA, four TWSA were integrated with a remotely operated vehicle (ROV) to test its ability to detect front obstacles and evaluate motion location in Figure S1 (Supporting Information). The ROV's spatial coordinates and velocity were measured using a commercial motion capture system called Nokov. Specifically, the attack angles of sensors I and III are 0°, while the attack angles of sensors II, and IV are 90°. The ROV follows a specified path, as shown in **Figure 5a**. The TWSA output signal exhibits different frequency and amplitude characteristics based on the ROV's operating state and the near-field flow field. An adaptive dynamic model must be established to evaluate the operating state and near-flow field of the ROV. However, the coupling of complex flow-induced vibrations with the inherent vibrations of the whisker shaft results in a highly nonlinear response of the TWSA output signal. This complexity makes it challenging to establish the relationship between the signal and the ROV state using traditional statistical analysis. On the other hand, data-driven methods, such as DL methods, possess the ability to address inherent accounting for uncertainties in actual measurement data. Figure 5b illustrates the operational process of the ROV's state and near-field estimation, encompassing data prediction processing, learning-based modeling, and whisker-based state estimation. Due to the time dependence and spatial correlation of multi-unit signals, a hybrid model combining a convolutional neural network (CNN) and a long short-term memory (LSTM) network is employed to establish the mapping relationship between the UTWS signal and the underwater vehicle state. CNN extracts spatial characteristics from multi-sensor data, which are then processed by sequence regression utilizing LSTM networks to achieve ROV state prediction and detect front obstacles as shown in Figure 5b,c.

Figure 5b,c shows the voltage and STFT analysis of the TWSA output signal during ROV operation. The voltage amplitude and dominant frequency of sensors II and IV exhibited an increase from 0 to 2 s. Notably, the vibration response of the 90° attack angle whisker(Sensor IV) is almost identical to that of a single whisker, indicating that no significant mutual interference occurs between adjacent whiskers at this spacing. This trend indicates that the ROV has transitioned from stopping to starting operations. During the ROV's uniform linear motion from 3 to 10 s, sensors II and IV generate a periodic voltage signal with

a constant dominant frequency. The attack angle of sensors III and IV changes by 90° when the ROV turns from 11 to 13 s. Specifically, sensor 3 rotates from 0° to 90° and sensor IV rotates from 90° to 0°. The voltage amplitude and dominant frequency of sensors III and IV exhibit a positive correlation with changes in the angle of attack. In summary, the amplitude and dominant frequency of the TWSA's four sensors' output signal exhibit a strong correlation with the movement direction and velocity of the Underwater vehicle. By analyzing the frequency-domain signal through the trained DL model (Figure 5d,e), the state (velocity and direction) of the ROV can be accurately mapped as shown in Figure 5f,g. This method achieves a low verification RMSE of 0.023 and a verification loss of 0.001 (Figure 5h). Additionally, the trajectory is inferred from the time series data along with the anticipated velocity and direction. The real 3D trajectory and predicted 3D trajectory of ROV are shown in Figure 5i (also see Video S2, Supporting Information). The maximum error of the trajectory is 83 mm and the minimum error is 6 mm.

To assess the ability of TWSA for simultaneous near-field perception and localization of ROV, the ROV followed an L-shaped path. The underwater vehicle first moves along the x-axis and then changes direction to proceed along the y-axis. It is noteworthy that while the ROV is moving along the x-axis, an obstacle is positioned in front of it. However, when the ROV changes direction to move along the y-axis, there are no obstacles in its path. From 0 to 11 s, the ROV transitioned from startup to uniform linear motion along the x-axis as illustrated in **Figure 6a**. The TWSA was subjected to the combined effects of VIV and WIV. Notably, sensor III of TWSA, with an angle attack of 0°, effectively suppressed VIV, allowing a clearer observation of the impact of WIV on the TWSA. When an obstacle is present in front of the ROV, the output signal of sensor IV exhibits significant amplitude and frequency variations, as shown in Figure 6a,b. Conversely, when the ROV changes direction to move along the y-axis with no obstacles ahead, both the amplitude and frequency of sensor III significantly decrease. Besides, Figure 6c,d presents the predicted ROV motion angle, velocity, and path by the trained DL model, which slightly differ from the actual values (see Video S3, Supporting Information). The maximum error between the predicted trajectory and the actual trajectory is 71 mm, while the minimum error is 10 mm with a low verification RMSE of 0.02 and a verification loss of 0.001(Figure S11, Supporting Information). This demonstrates that the TWSA maintains steady trajectory estimation capability while simultaneously sensing obstacles. Overall, these TWSA-based state estimation and near-field estimation techniques show great application potential for ROV autonomous local navigation and obstacle avoidance.

4. Conclusion

In this work, a triboelectric whisker array is fabricated for simultaneous near-field perception and localization of unmanned underwater vehicles. Imitating the structure of seals' whiskers, the TWSA integrates contact-separated triboelectric nanogenerators to convert micro-disturbances into electrical signals. The device offers advantages such as a simple structure, a short response time of 19 ms, a high sensitivity of 0.2 V/ms^{-1}, and a signal-to-noise ratio of 58 dB. The TWSA can simultaneously

**ADVANCED
SCIENCE NEWS**

www.advancedsciencenews.com

**ADVANCED
MATERIALS
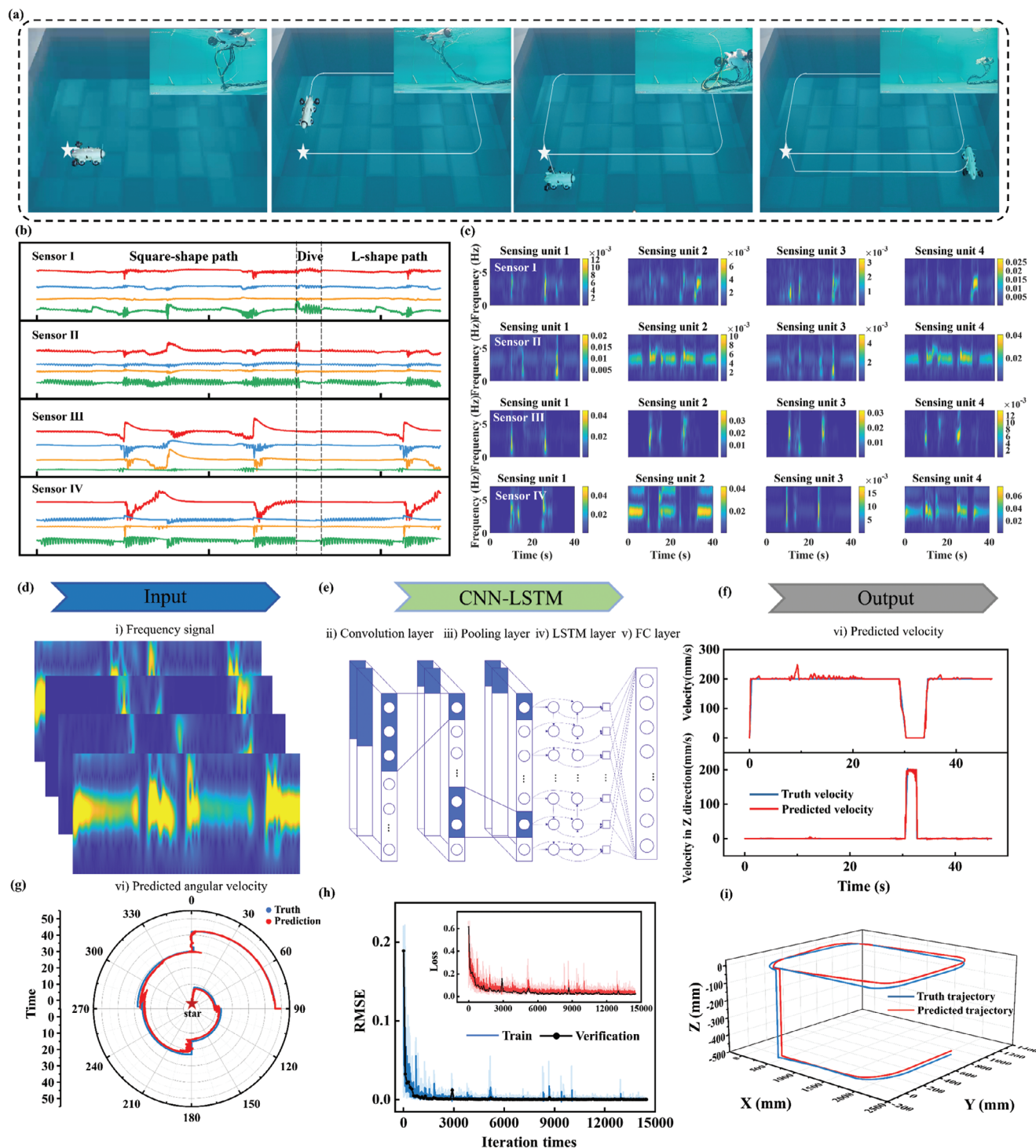TECHNOLOGIES**

www.advmattechnol.de

Figure 5. DL-assisted TWSA-based motion estimation of remotely operated vehicle (ROV). a) Motion trajectory of ROV. b) TWSA's output voltages. c) Fundamental frequency of the TWSA's voltage signal. d,e) Learning process of the ROV's state estimation. f) Truth velocity and the predicted volocity based on TWSA. g) The rate of rotational movement of the ROV throughout its motion path. h) The root-mean-square deviation and training data loss. i) Actual path and speed versus the estimated path and speed using TWSA.
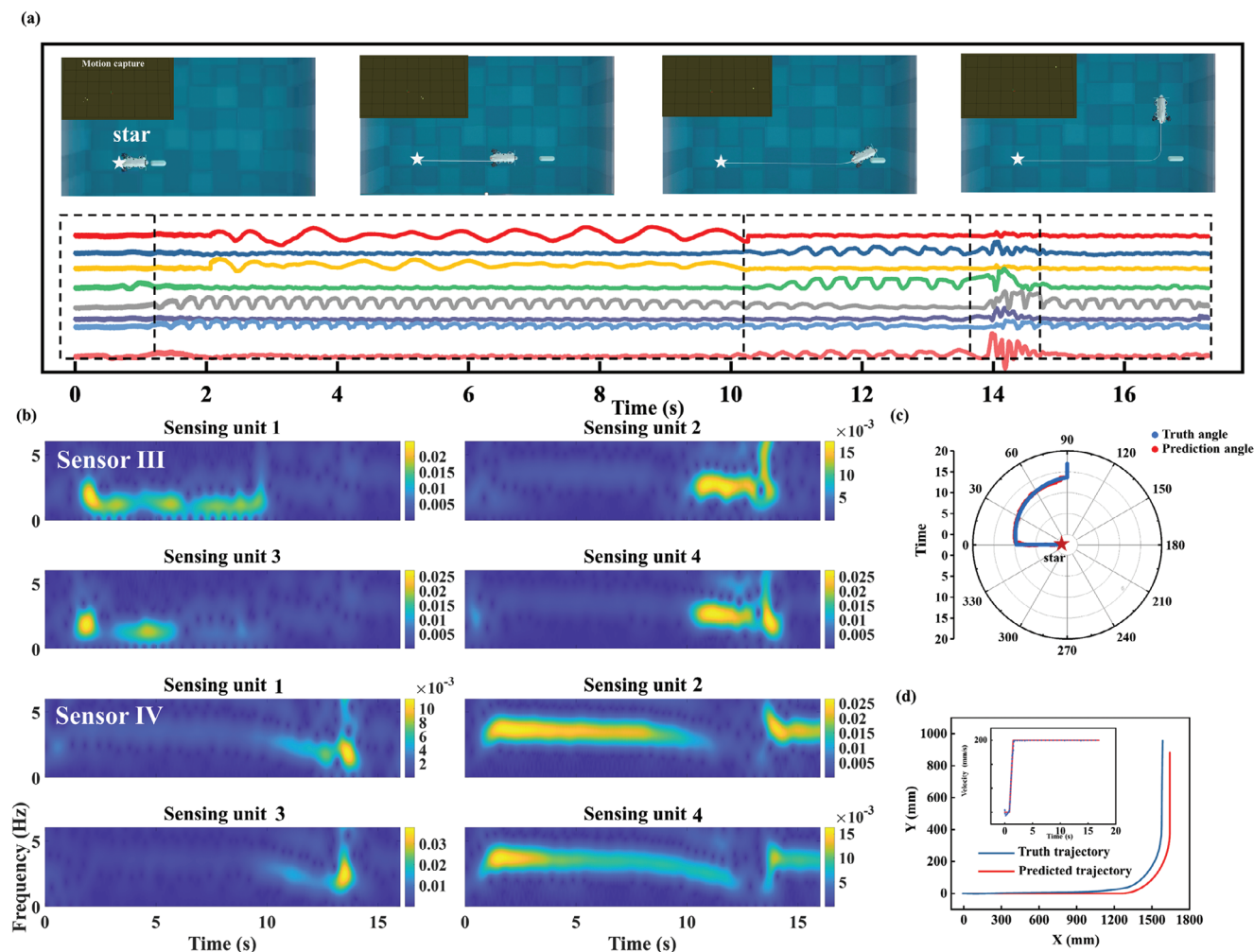
**ADVANCED
SCIENCE NEWS**

www.advancedsciencenews.com

**ADVANCED
MATERIALS
TECHNOLOGIES**

www.advmattechnol.de

Figure 6. DL-assisted TWSA-based Simultaneous near field perception and motion estimation of ROV. a) Motion trajectory of underwater vehicle and TWSA's output voltages. b) Spectrogram of TWSA's voltage signal. c) The rate of rotational movement of the ROV throughout its motion path. d) Truth trajectory and velocity, and the predicted trajectory and velocity based on TWSA.

obtain multiple types of near-field information, including the flow velocity and attack angle of the flow field and the wake information in the three-dimension. Notably, experiments have demonstrated a mapping relationship between the flow velocity and the output signals of the whisker array. Besides, the device also locks the frequency of the upstream wake vortex, with a minimal detection accuracy of 81.2%. Furthermore, the TWSA was fixed on the ROV, enabling path estimation and upstream wake perception through DL processing of the multi-channel signal. Achieving the RMSE of the validation data is ≈0.02. This study demonstrates that whisker-based perception via the DL-assisted TWSA equipped with the unmanned underwater vehicle can provide effective near-flow field information, assisting unmanned underwater vehicles in completing localized navigation operations.

Supporting Information

Supporting Information is available from the Wiley Online Library or from the author.

Conflict of Interest

The authors declare no conflict of interest.

Data Availability Statement

Research data are not shared.

[1] H. Ghafoor, Y. Noh, *Ieee Access* **2019**, *7*, 98841.

[2] S. Teng, A. Liu, X. Ye, J. Wang, J. Fu, Z. Wu, B. Chen, C. Liu, H. Zhou, Y. Zeng, J Yang, *Eng. Struct.* **2024**, *308*, 117958.

[3] J. Teague, M. J. Allen, T. B. Scott, *Ocean Eng.* **2018**, *147*, 333.

[4] D. R. Yoerger, A. F. Govindarajan, J. C. Howland, J. K. Llopiz, P. H. Wiebe, M. Curran, J. Fujii, D. Gomez-Ibanez, K. Katija, B. H. Robison, et al., *Sci. Rob.* **2021**, *6*, eabe1901.

[5] K. Sun, W. Cui, C. Chen, *Sensors* **2021**, *21*, 7849.

[6] S. Chutia, N. M. Kakoty, D. Deka, in *Proceedings of the 2017 3rd International Conference on Advances in Robotics*, Association for Computing Machinery, New York **2017**, pp. 1–6.

[7] J. Folkesson, J. Leonard, J. Leederkerken, R. Williams, in *IEEE/RSJ International Conference on Intelligent Robots and Systems*, IEEE, New York **2007**, pp. 3678–3684.

[8] C. White, D. Hiranandani, C. S. Olstad, K. Buhagiar, T. Gambin, C. M. Clark, *J. Field Robot.* **2010**, *27*, 399.

[9] D. Q. Huy, N. Sadjoli, A. B. Azam, B. Elhadidi, Y. Cai, G. Seet, *Ocean Eng.* **2023**, *267*, 113202.

[10] J. Guo, M. Fu, X. Liu, B. Zheng, *Opt. Eng.* **2023**, *62*, 038107.

[11] W. Feng, Y. Yi, S. Li, Z. Xiong, B. Xie, Z. Zeng, *Opt. Commun.* **2024**, *552*, 130106.

[12] M. Shwetha, S. Krishnaveni, *J. Interconnect. Netw.* **2024**, 2330001.

[13] S. Zhang, J. Wu, T. Yin, *Front. Mar. Sci.* **2023**, *10*, 1279693.

[14] T. Wang, T. A. Kent, S. Bergbreiter, *arXiv preprint arXiv:2307.09569* **2023**.

[15] X. Zheng, A. M. Kamat, M. Cao, A. G. P. Kottapalli, *Adv. Sci.* **2023**, *10*, 2203062.

[16] H. Bleckmann, R. Zelick, *Integr. Zool.* **2009**, *4*, 13.

[17] J. Liu, P. Xu, B. Liu, Z. Xi, Y. Li, L. Guo, T. Guan, P. Zhu, Z. Meng, S. Wang, H. Wang, M. Xu, *Small* **2023**, 2308491.

[18] M. Haggard, M. J. Chacron, *PLoS Comput. Biol.* **2023**, *19*, e1010938.

[19] J. Bunjevac, J. Turk, A. Rinehart, W. Zhang, *J. Vis.* **2018**, *21*, 597.

[20] H. Zaher, H. Al-Wahsh, M. Eid, R. S. Gad, N. Abdel-Rahim, I. M. Abdelqawee, *Alex. Eng. J.* **2023**, *80*, 88.

[21] C. T. Murphy, C. Reichmuth, W. C. Eberhardt, B. H. Calhoun, D. A. Mann, *Sci. Rep.* **2017**, *7*, 8350.

[22] G. Liu, Y. Jiang, P. Wu, Z. Ma, H. Chen, D. Zhang, *Soft Robotics* **2023**, *10*, 97.

[23] W. C. Eberhardt, B. F. Wakefield, C. T. Murphy, C. Casey, Y. Shakhsheer, B. H. Calhoun, C. Reichmuth, *Bioinspir. Biomim.* **2016**, *11*, 056011.

[24] S. Na, J. Park, N. Jones, N. Werely, A. Flatau, *Smart Mater. Struct.* **2018**, *27*, 105010.

[25] P. Xu, X. Wang, S. Wang, T. Chen, J. Liu, J. Zheng, W. Li, M. Xu, J. Tao, G. Xie, *Research* **2021**, *2021*, 9864967.

[26] X. Wang, J. Liu, S. Wang, J. Zheng, T. Guan, X. Liu, T. Wang, T. Chen, H. Wang, G. Xie, P. Xu, J. Tao, M. Xu, *Adv. Mater. Technol.* **2022**, *7*, 2101098.

[27] Z. L. Wang, J. Chen, L. Lin, *Energy Environ. Sci.* **2015**, *8*, 2250.

[28] Z. L. Wang, T. Jiang, L. Xu, *Nano Energy* **2017**, *39*, 9.

[29] Q. Shen, X. Xie, M. Peng, N. Sun, H. Shao, H. Zheng, Z. Wen, X. Sun, *Adv. Funct. Mater.* **2018**, *28*, 1703420.

[30] Z. Wang, J. Liu, Z. Wang, C. Liu, Q. Chen, C. Zhang, W. Zhang, J. Si, X. Xiao, P. Xu, M. Xu, *Nano Res.* **2024**, *17*, 6518.

[31] P. Xu, J. Zheng, J. Liu, X. Liu, X. Wang, S. Wang, T. Guan, X. Fu, M. Xu, G. Xie, M. Xu, Z. L. Wang, *Research* **2023**, *6*, 0062.

[32] M. Weng, J. Zhou, P. Zhou, R. Shang, M. You, G. Shen, H. Chen, *Adv. Sci.* **2024**, *11*, 2309846.

[33] P. Xu, J. Liu, X. Liu, X. Wang, J. Zheng, S. Wang, T. Chen, H. Wang, C. Wang, X. Fu, G. Xie, J. Tao, M. Xu, *npj Flexible Electron.* **2022**, *6*, 25.

[34] H. Wang, R. Shang, J. Chen, X. Jin, K. Chen, B. Huang, H. Chen, Q.-L. Lu, *Nano Energy* **2024**, *128*, 109843.

[35] X. Cai, Y. Xiao, B. Zhang, Y. Yang, J. Wang, H. Chen, G. Shen, *Adv. Funct. Mater.* **2023**, *33*, 2304456.

[36] H. Lei, Z.-Y. Yin, P. Huang, X. Gao, C. Zhao, Z. Wen, X. Sun, S.-D. Wang, *Adv. Funct. Mater.* **2024**, 2401913.

[37] L. Yuan, L. Zhao, H. Zhang, H. Liu, Y. Zong, X. Ding, J. Zhang, *Adv. Mater. Technol.* **2024**, 2400338.

[38] T. Zhao, L. Yuan, H. Liu, H. Zhang, J.-S. Dai, T. Li, J. Li, J.-H. Zhang, *IEEE Electron Device Lett*, IEEE, New York **2023**.

[39] X. Wang, Y. Shi, P. Yang, X. Tao, S. Li, R. Lei, Z. Liu, Z. L. Wang, X. Chen, *Small* **2022**, *18*, 2107232.

[40] Y. Zhang, Y. Li, R. Cheng, S. Shen, J. Yi, X. Peng, C. Ning, K. Dong, Z. L. Wang, *Research* **2022**, *2022*, 9809406.

[41] W. Wang, C. Zhao, Z. Wang, B. Mao, H. Wang, Y. Zhang, Z. Xi, C. Xiang, M. Xu, J. Qu, *IEEE Sens. J.* **2024**, *24*, 18928.

[42] S. Wang, P. Xu, X. Wang, J. Zheng, X. Liu, J. Liu, T. Chen, H. Wang, G. Xie, J. Tao, M. Xu, *Nano Energy* **2022**, *97*, 107210.

[43] L. Guo, J. Liu, G. Wu, P. Xu, S. Wang, B. Liu, Y. Li, T. Guan, H. Wang, J. Si, T. Du, M. Xu, *Sens. Actuators A* **2024**, *365*, 114875.

[44] G. Liu, W. Jiang, X. Zheng, Q. Xue, *Bioinspir. Biomim.* **2021**, *17*, 016004.

[45] A. Rinehart, V. Shyam, W. Zhang, *Bioinspir. Biomim.* **2017**, *12*, 066005.

[46] X. Zheng, A. M. Kamat, M. Cao, A. G. P. Kottapalli, *J. R. Soc., Interface* **2021**, *18*, 20210629.